

Improved Cycling Performance of High-Nickel NMC by Dry Powder Coating with Nanostructured Fumed Al_2O_3 , TiO_2 , and ZrO_2 : A Comparison

Marcel J. Herzog,^{*[a, b]} Daniel Esken,^[b] and Jürgen Janek^{*[a]}

Surface coating is an effective concept to protect layered cathode active materials (CAMs) in lithium ion batteries from detrimental side reactions. Dry powder coating is a fast and cost-effective coating process, and here we transfer this coating approach from Al_2O_3 to nanostructured fumed TiO_2 and ZrO_2 coatings on the same NMC ($\text{Li}[\text{Ni},\text{Mn},\text{Co}] \text{O}_2$) material. Using similar processing, this allows a direct comparison of the characteristics of the achieved coating layers and their influence on the cycling performance of high-nickel NMC. The nanostructured small oxide aggregates result in a quite homogeneous coating layer with a certain porosity around each CAM particle. Significantly enhanced long-term cycling stability is observed, with a trend of increasing stability in the series

$\text{ZrO}_2 < \text{TiO}_2 < \text{Al}_2\text{O}_3$. Fumed Al_2O_3 and TiO_2 coating layers prevent cathode particle cracking and disintegration successfully, while fumed ZrO_2 only shows a moderate protection effect. Each coating material enhances the rate performance compared to uncoated NMC in the row $\text{TiO}_2 < \text{ZrO}_2 < \text{Al}_2\text{O}_3$. XPS measurements of cycled electrodes indicate a partial incorporation of lithium ions in the crystalline TiO_2 and ZrO_2 coating layers, contributing to the enhanced lithium-ion transport across the CAM surface layer, as observed before for fumed γ - Al_2O_3 coatings. Summarizing the results, the best overall cycling performance was achieved by coating high-nickel NMC with fumed Al_2O_3 , providing the highest rate capability and the best long-term cycling stability.

1. Introduction

Cathode active materials (CAMs) suffer from several electrochemical degradation reactions, leading to a performance loss and aging during cycling.^[1–8] This is especially relevant for high-nickel layered NMC phases ($\text{LiNi}_x\text{Mn}_y\text{Co}_z\text{O}_2$ with $x+y+z=1$ and $x>0.5$), which are the most promising candidates to meet the rising requirements on CAMs for future lithium-ion batteries (LIBs).^[1,3–5,9–14] The high nickel content provides a higher specific capacity and relatively lower costs compared to cobalt-rich materials.^[1,9,13,15]

There are three strategies to stabilize the cycling performance of positive electrode materials, which are not mutually exclusive. *Bulk doping* is one effective method to enhance the stability of cathode materials. Metal or non-metal ions are doped into the bulk phase of the cathode material to stabilize

the crystal structure and to facilitate the lithium ion transfer kinetics.^[16–21]

Another one is the *core-shell* strategy, whereby a core of a highly reactive cathode material is covered by an outer sphere of a less reactive cathode material.^[22–24] This enables to combine the excellent stability of the shell material with the high electrochemical performance of the core material.^[25,26] To avoid harmful mechanical stress between the core and shell due to different volume expansion behavior during charging and discharging,^[27] the differences in chemical composition and crystal structural mismatch can be minimized by applying a concentration gradient.^[22,24] One disadvantage of this strategy could be the thick shell up to 2 μm , limiting the rate of lithium-ion and electron transportation.^[1]

Surface coating has proven to be an effective method to protect the reactive surface of CAMs from detrimental side reactions. The coating layer forms a physical barrier between CAM and electrolyte, and the decomposition of liquid electrolyte and deposition of decomposition products at the interface, which otherwise leads to increased resistance, is prevented.^[1,3–5,21] Additionally, coating layers can protect CAMs effectively against the attack of corrosive HF, formed by the reaction of the conducting salt LiPF_6 with trace amounts of H_2O . The acidic HF leads to dissolution of transition metal ions out of the surface of the CAM and causes lattice damage.^[2,3,6,7] As consequences, surface transformations as well as transition metal rearrangement destabilize the crystal structure,^[9–12,28] initiate cracks within the cathode secondary particles and cause subsequent particle disintegration.^[14,29] This causes loss of inner particle connectivity and gives rise to increased polarization,

[a] M. J. Herzog, Prof. Dr. J. Janek
Institute of Physical Chemistry & Center for Materials Research,
Justus-Liebig-University Giessen,
Heinrich-Buff-Ring 17, 35392 Giessen, Germany
E-mail: juergen.janek@phys.chemie.uni-giessen.de

[b] M. J. Herzog, Dr. D. Esken
Evonik Operations GmbH,
Rodenhäuser Chaussee 4, 63457 Hanau-Wolfgang, Germany
E-mail: marcel.herzog@evonik.com

 Supporting information for this article is available on the WWW under
<https://doi.org/10.1002/batt.202100016>

 © 2021 The Authors. *Batteries & Supercaps* published by Wiley-VCH GmbH.
This is an open access article under the terms of the Creative Commons Attribution Non-Commercial NoDerivs License, which permits use and distribution in any medium, provided the original work is properly cited, the use is non-commercial and no modifications or adaptations are made.

contributing to the degradation of performance and capacity fade.^[1,30]

Various techniques have been used to apply thin coating layers on CAM-surfaces, like wet-chemical deposition,^[5,31,32] sol-gel deposition,^[33,34] atomic layer deposition (ALD),^[35–37] physical vapor deposition (PVD)^[38] and chemical vapor deposition (CVD).^[39–41] Methods involving solvents produce waste, require an additional filter step and subsequent heating/drying processes, which may be unwanted in terms of economic and environmental sustainability. Gas phase deposition methods are expensive and hard to scale-up for industrial use.^[24] In comparison, dry powder coating is a simple, fast, cost effective and environmentally friendly approach for CAMs, which can easily be scaled-up to industrial use. CAM particles (micron-sized) are coated directly with submicron-sized particles (coating material) by using mechanical forces in a high energy mixer (e.g., Somakon MP-GL), without using any solvents and binders.^[42–44] The major challenge is to identify suitable starting materials for the coating process. In previous work,^[45] fumed metal oxides with specially synthesized nanostructured aggregates of small size have proven to be particularly suitable as precursors for an effective coating.

In our previous report,^[45] we presented a dry powder coating process for high-nickel NMC with fumed nanostructured Al₂O₃. The fumed metal oxide was found to adhere well on the surface of NMC secondary particles, even without an additional sintering process to fix the particles on the surface of the CAM. An almost continuous coating layer with a high coverage was achieved. The resulting coating layer showed a certain porosity, containing channels and holes. We assume that these channels are easily penetrated by the liquid electrolyte. This would significantly reduce the impedance of the otherwise insulating Al₂O₃ coating layer and explain the excellent lithium ion diffusivity observed. A significant increase in capacity retention, cycle life and rate performance of the Al₂O₃ coated NMC material was observed. Detrimental side reactions, resulting in a decreased CEI (cathode-electrolyte interphase) and charge transfer impedance during cycling were prevented. We attribute this enhanced cycling performance to the successful protection of the reactive surface of the CAM. In fact, we observed strong indication for incorporation of lithium ions into the crystalline γ-Al₂O₃, probably contributing to the enhanced rate capability.

A large number of reports on metal oxide coatings of CAMs have been published. The most commonly used oxides are, among others: SiO₂,^[32] Al₂O₃,^[33,35,37,46] TiO₂,^[47] V₂O₅,^[5] ZrO₂,^[34,35] ZnO,^[36] MgO,^[35] Co₃O₄,^[48] CeO₂.^[31] A direct comparison of the influence of different metal oxides on the cycling performance of CAMs is often not possible from literature. Thus, it is not unequivocally evident which metal oxide is the most suitable for a given type of CAM. Different coating methods as well as different cycling protocols are mostly applied in any of the reports, and observed performance differences can hardly be rationalized. Different coating methods result in different coating characteristics, like thickness and homogeneity of the coating layer, coverage of the surface, structure of the coating material, etc. Additionally, different CAMs were used in these

studies, which makes a direct comparison even more difficult. Even when the nominally same type of CAM is used, the cycling behavior strongly varies from producer to producer.

To date, dry powder coating of high-nickel NMC material is only described in literature with Al₂O₃ as coating agent. In this article, we report about dry powder coating with nanostructured fumed TiO₂ and ZrO₂. This enables a direct comparison of the characteristics of the coating layers and their influence on the cycling performance of otherwise identical high-nickel NMC. Each coated NMC shows a significantly enhanced rate capability, as well as long-term cycling stability. Investigations of cycled electrodes reveal that Al₂O₃, TiO₂ and ZrO₂ coating layers prevent cathode particle cracking, and indicate partial incorporation of lithium ions in the crystalline TiO₂ and ZrO₂ coating layers, like it was observed for fumed γ-Al₂O₃ coatings before.^[45] In conclusion, the developed dry coating approach is a very effective method to enhance the cycling performance of LIBs and to prolong their lifetime. The simple scalability to large scale high intensity mixers makes this process very suitable for industrial manufacturing. Furthermore, the coating process can be transferred to other types of CAMs and coating agents.

Experimental Section

Commercial NMC701515 (LiNi_{0.70}Mn_{0.15}Co_{0.15}O₂) powder (obtained from Linyi Gelon LIB Co.) and nanostructured fumed Al₂O₃, ZrO₂ and TiO₂ ("AEROXIDE® Alu 130", "VP ZrO₂" and "AEROXIDE® TiO₂ P90" from Evonik Operations GmbH) were used. A lab scale high energy mixer from Somakon Verfahrenstechnik UG (Somakon MP-GL) was used for carrying out the dry coating process. The mixing unit of the Somakon mixer consists of two very high-speed rotating rotors with 4 blades each and has a volume of 0.5 L. This process can easily be transferred to large scale industrial mixers (e.g. up to a mixer size of 3000 L from Eirich GmbH). For dry coating, the NMC-powder was mixed with 1.0 wt-% of the respective fumed metal oxide powder in the high energy mixer at first for 1 min at 500 rpm to homogeneously mix the two powders. Afterwards the mixing intensity was increased to 2000 rpm for 6 min to de-agglomerate the nanostructured fumed metal oxide into smaller aggregates that adhere at the surface of NMC. The coated CAM is used as received after mixing process, it is not further calcined.

Characterization

Scanning electron microscopy (SEM)

The particles and their morphology were investigated with a "JSM-7600F" SEM from Jeol. The accelerating voltage was set to 1 kV, and the beam current was 30 pA. A graphite tape was used to attach the samples on the sample holders. Electron-dispersive X-ray spectroscopy (EDX) measurements were conducted with an equipped X-Max 150 mm² detector (Oxford Instruments) and processed with Aztec-software. Therefore, the accelerating voltage and beam current were increased to 20 kV and 500 pA, respectively. The cross sections of the cycled electrodes were prepared by embedding the electrodes in an organic resin and subsequent cutting via microtomy.

X-ray powder diffraction (XRD)

The X-ray diffraction patterns were recorded with a Cubix3 Pharma diffractometer with a X'Celetor detector. Cu-K α radiation was employed to identify the crystal structure of the powders in the 2 θ range from 5° to 100° with a step size of 0.02° and a count time of 40 s.

Surface area measurements (BET)

Single point BET measurements were conducted using a Micromeritics TriStar 3000 with a nitrogen/helium flow (28.6% N₂). The samples were degassed at 150 °C for 20 min before the measurement.

Transmission electron microscopy (TEM)

The cross section TEM lamellae were cut from a NMC spherical particle covered by the respective fumed metal oxide. The cross-sectional cuts of the sample were prepared via focused ion beam (FIB) using a Fei Helios 650 dual-beam Focused Ion Beam device. During the preparation process, carbon and platinum protective layers were deposited on top of the film. TEM images were acquired on a double aberration-corrected Fei Titan³ 80–300 electron microscope operated at 300 kV in monochromated mode, providing an energy resolution of 150 meV. Before the TEM experiments, the specimen was cleaned through plasma cleaning.

X-ray photoelectron spectroscopy (XPS)

XPS measurements were conducted on cycled cathodes in discharged state. The cells were opened under argon atmosphere and the cathodes were washed with ethyl methyl carbonate to remove LiPF₆. Afterwards, the cathode was mounted on the XPS sample holder and transferred to the XPS analysis equipment without any exposure to air. The XPS measurements were conducted on an ESCALAB 250xi system from ThermoFisher Scientific, using an Al K α excitation source. The diameter of the measurement spot was 900 μ m. The graphite peak at 284.6 eV was used as a reference for the adjustment of the energy scale in the presented spectra. The resolution of the measurements was in general 0.1 eV.

Electrode and Cell Preparation

Electrodes for electrochemical measurements were prepared by blending 90 wt-% NMC with 5 wt-% PVDF (Solef PVDF 5130) as a binder and 5 wt-% Super PLi (Timcal) as a conductive additive under inert gas atmosphere. *N*-Methyl-2-pyrrolidone (NMP) was used as solvent. The slurry was casted on aluminum foil and dried for 20 min on a 120 °C heating plate in air. Afterward, the electrode

sheet was dried in a vacuum furnace at 120 °C for 2 h. Circular electrodes with a diameter of 12 mm were punched out, calendered with a pressure of 620 kPa and dried again in a vacuum furnace at 120 °C for 12 h to remove any residual water and NMP. The cathode loading for all samples was adjusted to 1.3–1.4 mAh cm⁻² (assuming a specific capacity of 180 mAh g⁻¹) or 7.0–8.0 mg_{NMC} cm⁻².

For the cycling tests the cells were assembled as CR2032 type coin cells (MTI Corporation) in an argon-filled glovebox (Glovebox Systemtechnik GmbH). Lithium metal (Rockwood Lithium GmbH) is used as anode material. Celgard 2500 was used as separator. 25 μ L of a solution of 1 molar LiPF₆ in ethylene carbonate and ethyl methyl carbonate (50:50 wt/wt; Sigma-Aldrich) was used as electrolyte. The cells were locked with a crimper (MTI).

Cell Cycling

Galvanostatic cycling was performed between 3.0 and 4.3 V vs Li⁺/Li at room temperature using a MACCOR battery cycler. For the calculation of the capacities and the specific currents, only the mass of the active material was considered. During cycling, the C-rate was increased every four cycles, starting from 0.1/0.1 (Charge/Discharge) to 0.3/0.3, 0.5/0.5, 1.0/1.0, 1.0/2.0 and 1.0/4.0 C. Afterward, the cell was cycled at 0.5/0.5 C for long-term stability test.

2. Results and Discussion

2.1. Dry-Coating Process

It is important to note the specific characteristics of the coating agents used for the dry powder coating. Fumed metal oxides are produced by flame hydrolysis and consist of agglomerated nanoparticles, having very high BET surfaces.^[49] The larger agglomerates can be split into smaller aggregates, which are built of primary particles nucleated in the flame, followed by growth processes (primary particle size of ~10–15 nm), that are chemically bonded together to form highly nanostructured three-dimensional entities with a more or less high degree of branching.^[49] Figure 1 shows scanning electron microscopy (SEM) images of single aggregates of the respective nanostructured metal oxide. These aggregates cannot easily be split into individual primary particles.^[49] All used fumed metal oxides in this study are crystalline (fumed Al₂O₃; γ -alumina, TiO₂; mostly anatase, ZrO₂; mostly tetragonal phase).

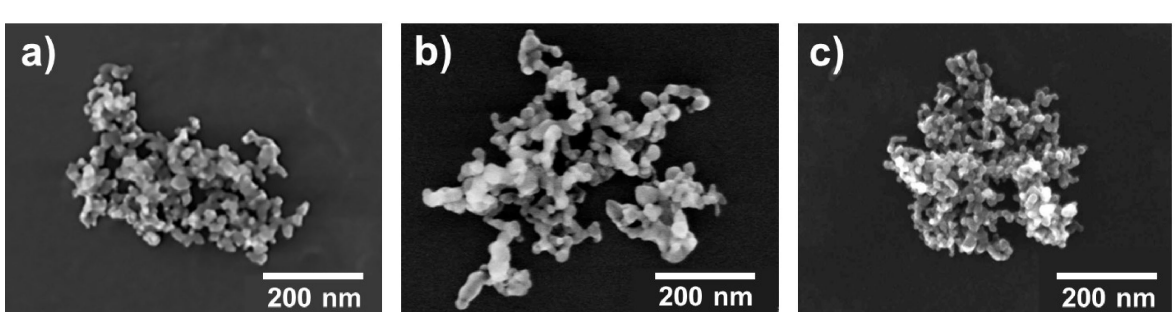


Figure 1. SEM-images of single aggregates of the respective fumed metal oxide: a) fumed Al₂O₃, b) fumed ZrO₂, c) fumed TiO₂.

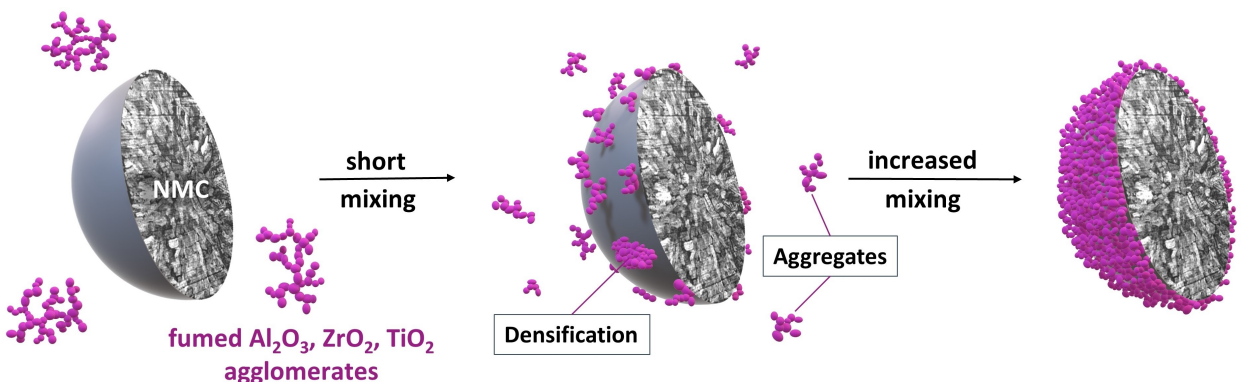


Figure 2. Schematic mechanism of the dry coating process in this study (cross-sectional view). The nanostructured fumed metal oxide is de-agglomerated into smaller aggregates during the high energy mixing process and interacts with the surface of the cathode powder. This de-agglomeration of the fumed metal oxide powder is the key of our dry coating method. After appropriate mixing, a quite continuous and strong adhesive coating layer is formed.^[45]

The principle of this dry coating process is shown in Figure 2. Micron-sized NMC particles are acting as core particles (host particles) and the submicron-sized nanostructured fumed metal oxides as the coating material (guest particles). During the high energy mixing process, nanostructured fumed metal oxide is de-agglomerated into smaller aggregates and starts to interact with the surface of the CAM. This de-agglomeration of the fumed metal oxide powder is decisive for the coating process. The small nanostructured aggregate size provides a high specific surface area and a good adhesion to the CAM particle surfaces. Since the size of coating material particles is very small, Van der Waals interactions or electrostatic interactions and the mechanical forces applied by the coating process are strong enough to keep them firmly attached to the core particles.^[44,50–52] It is important to understand that the coating layer consists of 3-dimensional nanostructured aggregates of different sizes with a specific branching and not of spherical uniform nanoparticles. At a given mixing energy, a certain degree of densification and coalescence of the aggregates at the cathode particle surfaces is achieved, resulting in a quite continuous and strong adhesive coating layer. An additional calcination step after dry coating for fixing the fumed oxide particles is not required, which is saving energy and costs. For a more detailed description of this dry coating process we refer to our previous article.^[45] In previous investigations, the best performance was achieved for the coating fraction of 1 wt-%.^[45] This quantity was adopted for the current investigations on fumed Al₂O₃, TiO₂ and ZrO₂.

2.2. Analysis of Coated Cathode Material

The X-ray powder diffraction (XRD) patterns of the coated NMCs are compared to uncoated NMC material in Figure 3. All diffraction peaks are indexed on the basis of the α -NaFeO₂ structure with a space group of $R\text{-}3\text{ }m$. There was no difference detected in the XRD signals of any coated NMC and uncoated NMC, indicating that the coating process is not influencing the original bulk crystal structure of the cathode material. No extra diffraction peaks of the thin coating layer are detected.

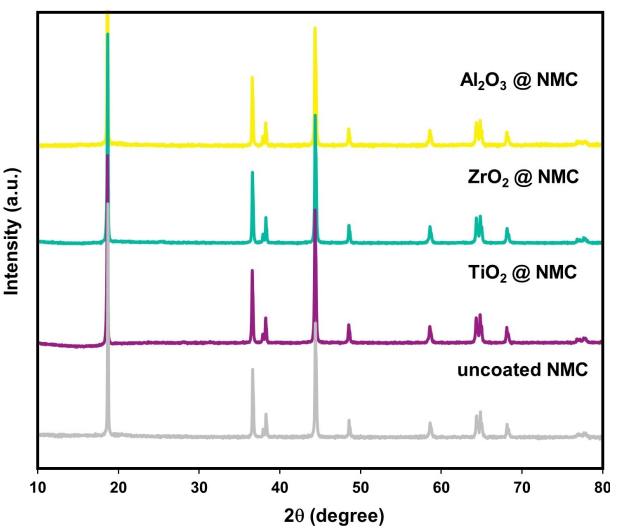


Figure 3. XRD patterns of NMC701515 coated by 1 wt-% fumed Al₂O₃, ZrO₂ and TiO₂ compared to uncoated NMC.

2.3. Characterization of the Coating Layer

The fumed Al₂O₃, TiO₂ and ZrO₂ coated NMC was investigated by scanning electron microscopy in combination with energy dispersive X-ray spectroscopy (SEM-EDX). Backscattered electrons (BSE) images (Figure 4a,b,c) show that the NMC particles are still intact despite the exposure to high shear forces in the mixing process. In all EDX mappings of the metal elements of the individual coatings a homogeneous coverage around all cathode particles was found (Figure 4d,e,f). No large, fumed metal oxide agglomerates were observed, showing that the de-agglomeration of all three kinds of nanostructured fumed metal oxides was successful. Additionally, no free unattached fumed metal oxide was found next to the cathode particles, indicating a strong adhesion between coating material and substrate.

Figure 5 shows high resolution SEM images of the surface of uncoated NMC (a) compared to NMC coated with 1 wt-% Al₂O₃ (b), ZrO₂ (c) and TiO₂ (d). The surface of the pristine NMC

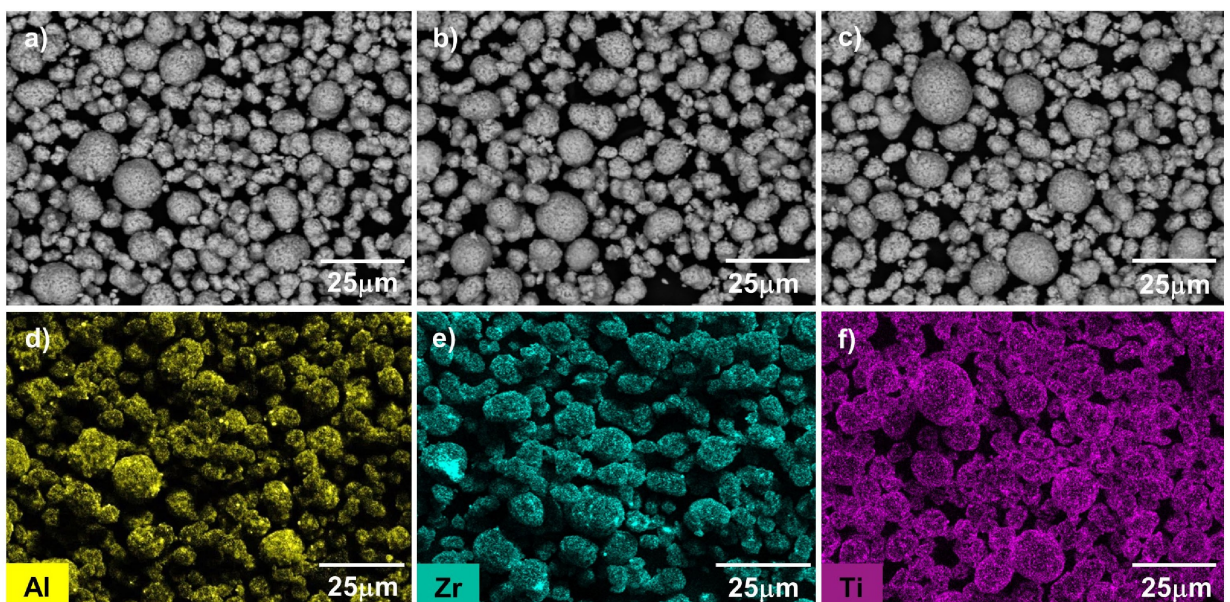


Figure 4. SEM-EDX images of NMC701515 coated by 1 wt-% of the respective fumed metal oxide: BSE images of NMC coated by Al_2O_3 (a), ZrO_2 (b) and TiO_2 (c) and EDX mapping of Al (d), Zr (e) and Ti (f).

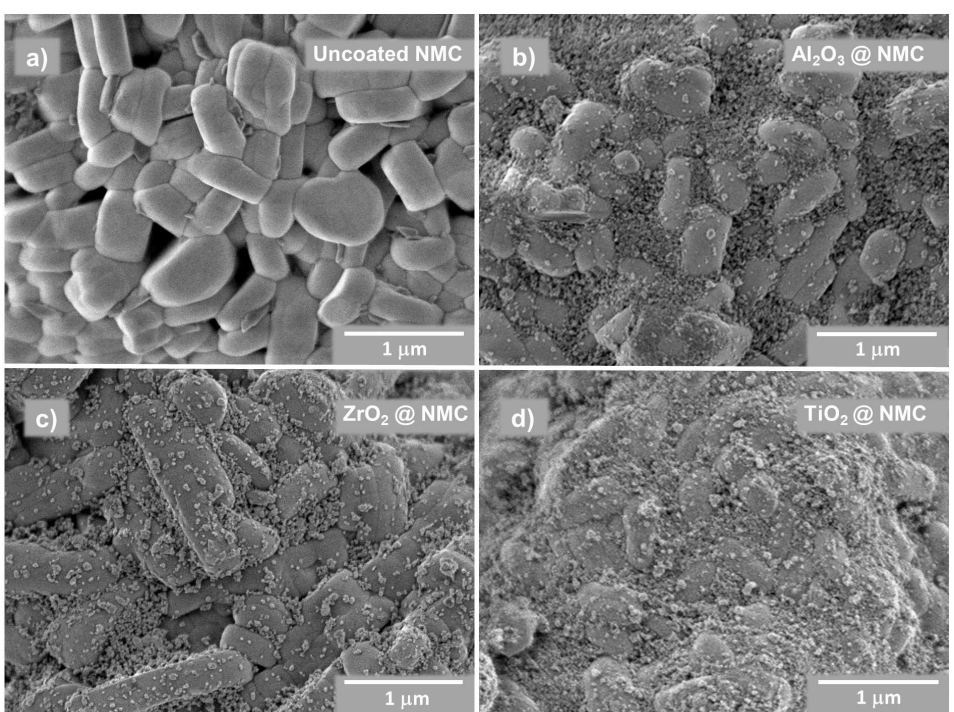


Figure 5. SEM images of the surfaces of uncoated NMC (a) and NMC701515 coated by 1 wt-% Al_2O_3 (b), ZrO_2 (c) and TiO_2 (d).

consists of small primary NMC crystallites with a very smooth and clean surface, composing the secondary particle structure. The surface of the secondary structure itself is rough having particles protruding from the plane and pits. The SEM images of all coated NMC surfaces reveal well how the coating material is distributed. The image of NMC coated with 1 wt-% Al_2O_3 (Figure 5b) shows a quite continuous coating layer, but the protruding crystallites are only partially covered or covered

only by a very thin layer, while the regions in between are fully filled up with the coating agent. By applying 1 wt-% ZrO_2 (Figure 5c) also a quite continuous coating layer is achieved, but in total a lower coverage of the CAM-surface is observed. However, the coating material distribution of ZrO_2 is more homogeneous in comparison to Al_2O_3 . The ZrO_2 coating material also predominantly accumulates in surface pits of the NMC, but they are less covered than in the case of the Al_2O_3

coating, while the surfaces of the protruding crystallites are more covered in the case of the ZrO_2 coating. With 1 wt-% TiO_2 (Figure 5d) an almost complete coverage of the surface by a continuous and dense coating layer is achieved. It should be noted that the degree of surface coverage by coating materials is influenced by different molecular masses of the used metal oxides (different molar amount of substances at same mass) and BET surfaces of the fumed materials. Low molar masses of coating compounds lead to higher molar amount of substance and higher BET surfaces lead to smaller aggregates. Both is tending to result in a higher degree of coverage of the surface. The BET surfaces of the used fumed metal oxides are shown in Table 1. In our test 1 wt-% of each coating metal oxide was used, due to different molar masses this results into different amounts of substances. The ratio of the amount of substances is $n_{\text{Al}_2\text{O}_3} / n_{\text{ZrO}_2} / n_{\text{TiO}_2} = 0.783 / 0.648 / 1.00$, which reflects the observed surface coverages in the SEM images.

For a more in-depth microstructure analysis, transmission electron microscopy (TEM) was performed. Figure 6 shows how the coating layers are structured. In all three cases, the coatings consist of aggregated small particles, which in turn consist of fused primary particles, accumulating at the surface of NMC and forming a partly porous layer. In contrast the uncoated NMC shows a clean and flat surface of a primary NMC crystallite. The porosity of the achieved coating layers is confirmed by BET measurements of the coated NMCs in comparison to the uncoated NMC as can be seen in Table 1.

Cross sections of manufactured electrodes before use in a battery cell were prepared and investigated by SEM-EDX analysis (Figure 7). The comparison of BSE images with EDX mappings of the coating metals reveals that the coating layer, for all three kinds of fumed metal oxides, is still intact and covers each individual CAM-particle. This demonstrates that all achieved coating layers remain stable during slurry preparation

and subsequent calendering in the cathode manufacturing process. An additional annealing step with high temperatures was not required to fix the coating particles at the NMC surface.

2.4. Electrochemical Characterization

To investigate the influence of the respective fumed metal oxide coatings on the cycling performance of high-nickel NMC, NMC coated with 1 wt-% Al_2O_3 , ZrO_2 and TiO_2 was evaluated in coin half-cells (with lithium metal anode). The cycling performance of coated materials are then compared with the performance of uncoated NMC and shown in Figure 8. To rule out that the dry coating process itself has an influence on the cycling performance, we compared the cycling performance of NMC, processed in the dry coating approach without coating agents, with the unprocessed pristine NMC. Hereby no significant changes in the performance were observed. The cycling data is presented in Figure S1 (supporting information). All three fumed metal oxide coatings clearly improve the cycling performance of high-nickel NMC. All coated NMC materials show slightly higher initial specific discharge capacities than bare NMC. We attribute this to a beneficial side effect of the stable coating layers, namely the improvement of the storage properties of high-nickel NMC by keeping off CO_2 and H_2O .^[53] High-nickel NMC tends to suffer from lithium loss upon formation of surface impurity compounds, mostly carbonates, resulting in a capacity decrease.^[54,55] This is discussed in more detail by analysis of voltage-capacity curves of initial charge profiles below.

At the beginning of the cycling sequence, the rate capabilities of the materials were evaluated. Therefore, the cells were discharged at different rates from 0.1 C to 4 C. The

Table 1. BET surfaces of the respective fumed metal oxides and the NMC dry coated by them.

	Al ₂ O ₃	ZrO ₂	TiO ₂
BET surface [m ² /g]	130	45	90
uncoated NMC	Al ₂ O ₃ @NMC	ZrO ₂ @NMC	TiO ₂ @NMC
BET surface [m ² /g]	0.48	1.5	0.85
			1.2

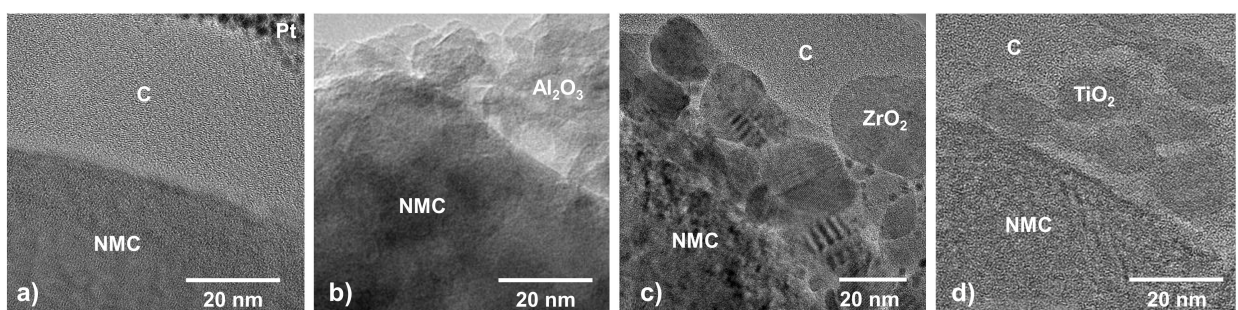


Figure 6. TEM images of a) uncoated NMC, b) NMC coated by 1 wt-% Al_2O_3 , c) NMC coated by 1 wt-% ZrO_2 and d) NMC coated by 1 wt-% TiO_2 . Carbon and platinum protective layers were deposited on top of the film for focused ion beam (FIB) preparation.

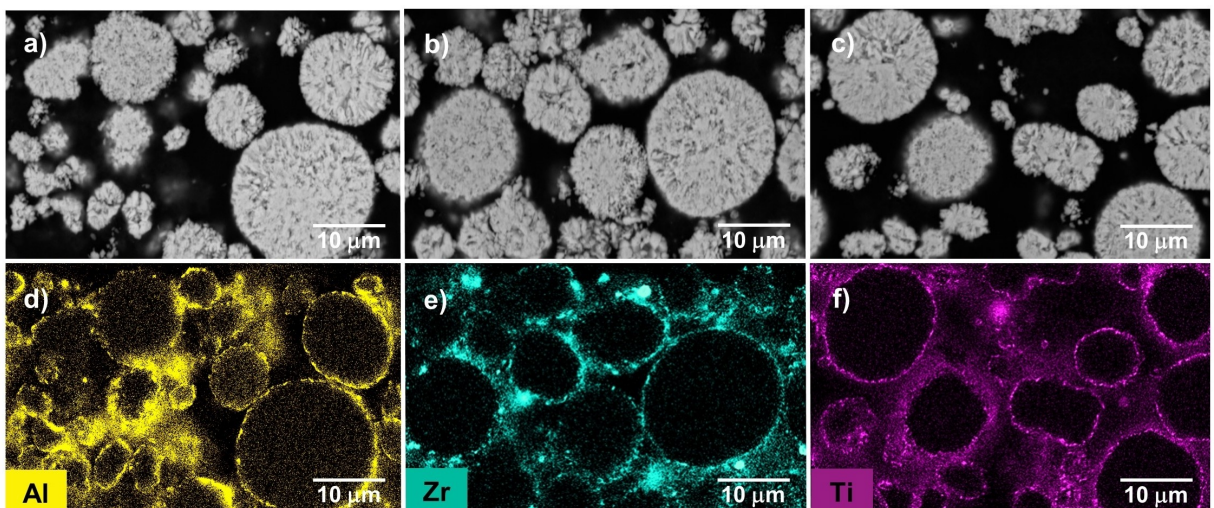


Figure 7. SEM images of cross sections of manufactured electrodes of NMC701515 dry coated by 1 wt-% fumed metal oxides: BSE images (a: Al_2O_3 -coated, b: ZrO_2 -coated and c: TiO_2 -coated NMC) and corresponding EDX mappings (d: Al, e: Zr and f: Ti) show that coating layers are still intact after electrode manufacturing process.

discharge curves at the different C-rates are shown in Figure 9. With increasing current density, the discharge capacities of the cathode electrodes gradually decrease for all samples, which results from limited lithium diffusion in the CAM secondary particles. With an increase of current density, the discharge capacities of all coated NMCs are superior to uncoated NMC. Clearly, the three coating layers show different effects on the rate capability of NMC cathodes. The best rate performance is observed with Al_2O_3 -coated NMC (discharge capacity of 134 mAh/g at rate of 4 C), while ZrO_2 -coated NMC (discharge capacity of 125 mAh/g at rate of 4 C) shows a slightly better rate performance compared to NMC with TiO_2 coating (discharge capacity of 115 mAh/g at rate of 4 C).

Our findings agree quite well with the results of Li *et al.*,^[56] who investigated the influence of Al_2O_3 , ZrO_2 and TiO_2 ALD coatings on LiCoO_2 . For TiO_2 and ZrO_2 coatings an increase in rate capability of the LiCoO_2 cathodes was found, while for the ZrO_2 coated CAM an enhanced effect on the rate performance improvement compared to TiO_2 was obtained. The data for the Al_2O_3 coating do not agree with our results. Li *et al.*^[56] observed no increasing rate performance using Al_2O_3 as coating material on LiCoO_2 , while we observed the best rate performance for Al_2O_3 -coated NMC.

As shown in a previous report,^[45] lithium ions tend to be incorporated in the fumed Al_2O_3 coating layer during cycling and form $\text{Li}_x\text{Al}_2\text{O}_3/\text{LiAlO}_2$, contributing to the significantly increased rate performance. XPS analysis, presented later in this article, also strongly indicates a lithium ion integration in fumed ZrO_2 and TiO_2 coating layers.

It is important to notice at this point that the applied amount of coating material has a significant influence on the rate performance, as we showed in our previous report.^[45] The best performance with Al_2O_3 -coatings was achieved when a coating mass fraction of 1 wt-% was applied. In this work, the fraction of coating agent was therefore set to 1 wt-% for better comparability. Consequently, the amount of coating material

for ZrO_2 - and TiO_2 -coated NMC is presumably not optimized to achieve the best rate performance, but it still allows conclusions on the rough trend. Coating layer thickness and coating layer porosity are important parameters influencing the rate performance of coated cathode materials. To achieve the best possible rate performance for ZrO_2 and TiO_2 coatings, a more detailed analysis to optimize these parameters would be necessary for each coating material, which is beyond this study. Nevertheless, a clear trend can be derived from the results.

Although lithium zirconate is attributed a significantly higher lithium ion conductivity than γ -lithium aluminate,^[57,58] we observed the highest rate capability for the fumed Al_2O_3 -coated NMC. However, as can be seen in Table 1, the BET surface area of the Al_2O_3 -coated NMC ($1.5 \text{ m}^2/\text{g}$) is significantly higher than that of the ZrO_2 -coated sample ($0.85 \text{ m}^2/\text{g}$). Obviously, a higher porosity is achieved with the Al_2O_3 coating layer. These results indicate a strong influence of the coating layer porosity, on the rate capability, which is a purely physical parameter. Assuming that the liquid electrolyte penetrates the porous coating layer, we suggest that the porosity of the coating has a significant influence on the lithium transport across the layer, besides the lithium diffusion coefficients of the coating materials themselves, since the diffusion coefficient of the liquid electrolyte is orders of magnitude higher than that of the lithiated metal oxides.^[57–61] Therefore, the rate performance of ZrO_2 coated NMC cannot be optimized by varying the mass fraction of ZrO_2 such that it reaches the performance of Al_2O_3 coated NMC. We attribute the lower rate performance in this case to inferior physical properties of the ZrO_2 coating layer. It is very likely that, when the coating layers of Al_2O_3 and ZrO_2 coated materials would have the same porosity, the rate performance of ZrO_2 -coated NMC would be superior. However, porosity cannot be influenced by variation of the coating fraction. For this purpose, the primary particle size has to be optimized towards smaller primary particles and higher BET surface areas, which will be part of future work.

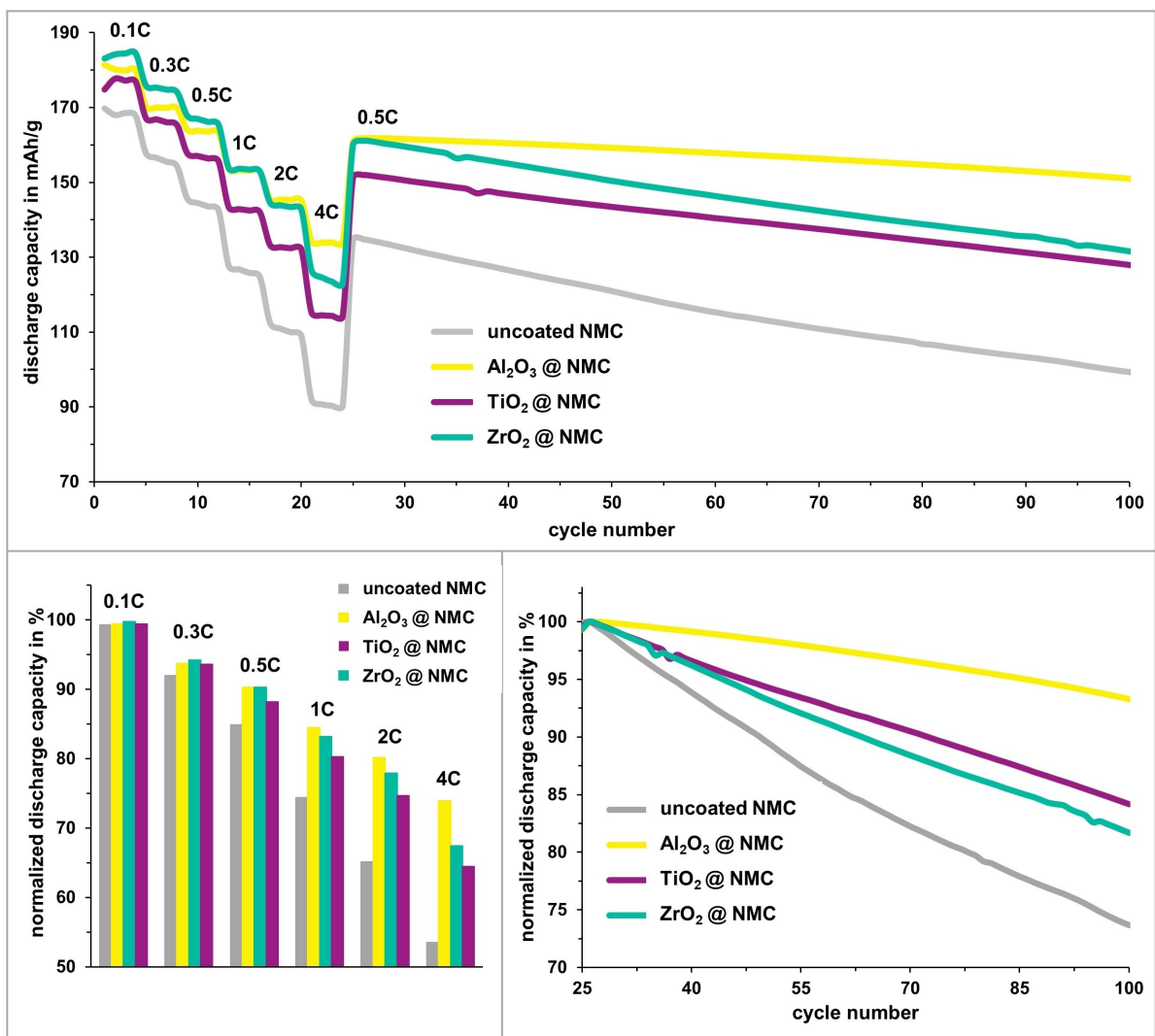


Figure 8. Cycling performance of NMC701515 dry-coated by the respective fumed metal oxides (1 wt-%) and uncoated NMC (average of 3 cells each): Absolute (top) and normalized (bottom; left: rate test, right: long-term cycling sequence) discharge capacities.

The porosities of Al_2O_3 and TiO_2 coating layers are in the same range, nevertheless, the rate performance of TiO_2 coated samples is significantly lower. By reducing the coating fraction of TiO_2 , the effective thickness of the coating layer will be reduced to a small extent, which then should enhance the rate performance to some extent. As the gap in rate performance between TiO_2 coated and Al_2O_3 coated NMC is large, it is unlikely that the rate performance of TiO_2 coated NCM can be improved to the extent that it can compete with the Al_2O_3 coating. Consequently, the superior rate performance of the Al_2O_3 coated NMC is attributed to favourable chemical properties of Al_2O_3 .

Even though a significantly higher porosity was achieved for the TiO_2 coated NMC ($1.2 \text{ m}^2/\text{g}$), a lower rate performance was observed compared to the ZrO_2 coated sample ($0.85 \text{ m}^2/\text{g}$). Optimization of the TiO_2 coating layer thickness could raise the rate performance of the two materials to almost the same level. Since the physical parameters of the ZrO_2 coating layer are

inferior and the rate performance can still compete with TiO_2 coated material, ZrO_2 is attributed superior chemical properties.

In comparison, the uncoated NMC delivers only 90 mAh/g at this rate. These results indicate that the solid electrolyte interface (SEI) formed by electrolyte decomposition products on the uncoated NMC surface during cycling has a higher lithium ion resistivity than the porous coating layers. Consequently, the coating layers successfully prevent decomposition of electrolyte on the surface of the cathode material and growth of a thick SEI layer during cycling.

After the rate test, a long-term cycling sequence was applied at a rate of 0.5 C (Figure 8). The highest improvement in cycling stability and capacity retention was achieved by coating with Al_2O_3 , showing a discharge capacity loss in long-term cycling of only 5.4% (from cycle 25 to cycle 100). For the ZrO_2 coated sample, slightly higher capacities were recorded overall compared to TiO_2 coated NMC, but the slope of capacity decrease is somewhat steeper (15.4% from cycle 25 to cycle 100 for ZrO_2 coated, compared to 13.1% for TiO_2 coated

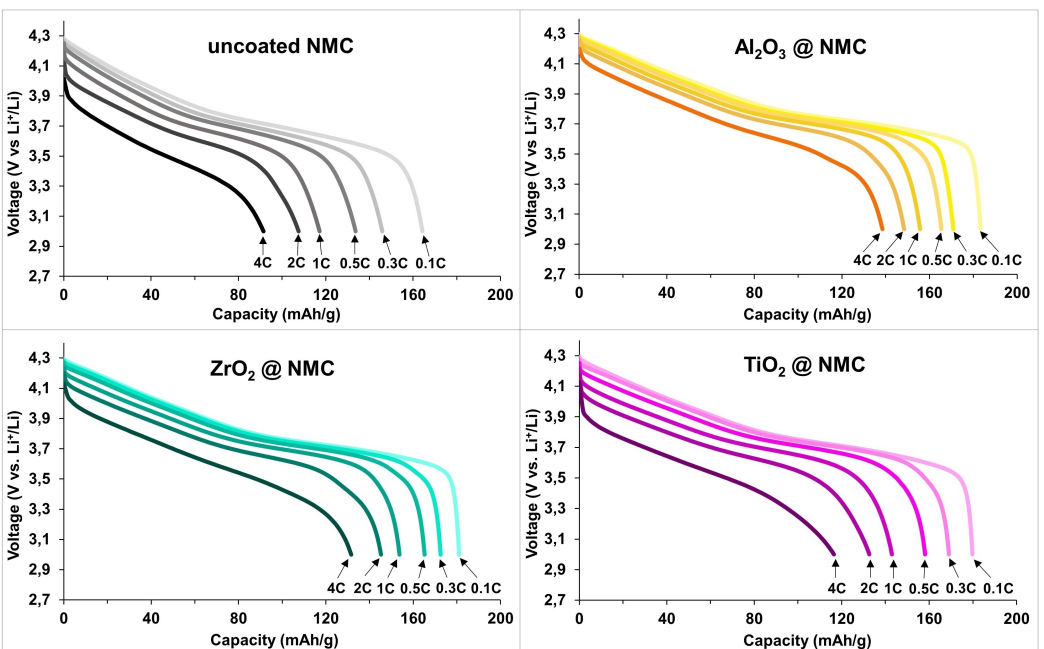


Figure 9. Galvanostatic discharge profiles of uncoated NMC and NMC coated by 1 wt-% fumed Al_2O_3 , ZrO_2 and TiO_2 cycled between 3.0–4.3 V at room temperature at various discharge rates.

NMC). In contrast, the capacity decrease of uncoated NMC is distinct, a capacity loss of 20.8% is detected. These findings again agree very well with the results of Li *et al.*^[56]

The improved cycling behavior of the coated CAMs is attributed to a successful protection of the reactive surface of the high-nickel cathode material from detrimental side reactions. The surface is shielded by fumed metal oxide coatings against electrolyte decomposition and the formation of a thick SEI layer, which would hinder the diffusion of Li^+ -ions and electrons, leading to capacity fading.^[62,63] Additionally, the attack of acidic HF, produced by LiPF_6 in the electrolyte, is also prevented due to the HF-scavenging effect of Al_2O_3 , ZrO_2 and TiO_2 .^[28,56,64–67] The dissolution of transition metal ions out of the surface of the cathode material into the electrolyte and the resulting lattice distortion in the cathode material, which is also an important reason for the decreasing capacity during charge–discharge processes, is thus inhibited.^[2,3,6,7]

The protection effect of high-nickel NMC-surfaces definitely depends on the chemical nature of the metal oxides used as coating agents and not only on the coverage of the CAM surface, whereby a higher degree of surface coverage results in improved long-term cycling stability due to less uncovered and reactive surface areas. This chemical protection effect seems to be strongest for Al_2O_3 as coating material.

Although the surface coverage of the ZrO_2 coated sample is lower compared to Al_2O_3 coated NMC and can be increased by optimization of the coating fraction, it is improbable that ZrO_2 coated NMC reaches the long-term cycling stability of Al_2O_3 coated NMC, since the gap in the long-term cycling performance of both samples is large. Additionally, it is established that lithium ions migrate preferably along grain boundaries in NMC secondary particles, because of a low diffusion energy barrier,

providing a fast diffusion pathway.^[68,69] Especially in these important regions, the coverage by the coating material is very high for all coating agents. Therefore, a further increase in surface coverage is expected to have a rather small influence on the long-term cycling performance. Therefore, we attribute to Al_2O_3 a more pronounced protection effect for CAM surfaces than to ZrO_2 , due to the chemical nature of the materials.

The TiO_2 coated NMC already shows an almost full coverage of the surface, and we know from previous studies,^[45] that a too thick coating layer results in decreased long-term cycling stability. Therefore, the long-term cycling stability of TiO_2 coated NMC cannot be further enhanced significantly by adjusting the coating fraction. Consequently, it is impossible that the TiO_2 coated NMC exceeds the Al_2O_3 coated NMC in the long-term cycling stability. This is again attributed to the superior protection effect of Al_2O_3 due to its chemical properties.

Since the surface coverage of ZrO_2 coated NMC is significantly lower compared to TiO_2 coated NMC and the gap in the long-term cycling performance is not distinctive, it can be hardly concluded whether the long-term cycling stability of ZrO_2 -coated NMC can exceed the one of TiO_2 coated NMC by adjusting the physical parameter of surface coverage. This will be investigated in further studies.

Summarizing, the optimal coating agent to achieve the best overall cycling performance for this investigated NMC701515 is 1 wt-% of Al_2O_3 , combining good rate capability with high capacity retention.

Figure 10 shows the voltage vs. capacity profiles of charge and discharge curves of uncoated and NMC coated by 1 wt-% Al_2O_3 , ZrO_2 and TiO_2 cycled between 3.0 and 4.3 V. In the first charging profile of the uncoated NMC (Figure 10a), an initial

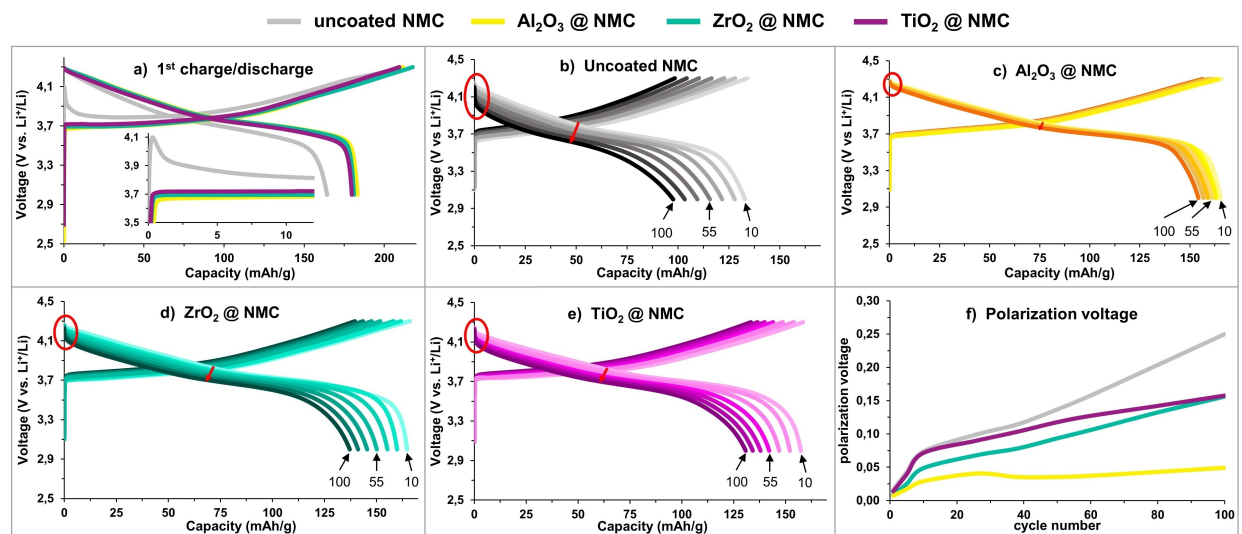


Figure 10. Galvanostatic charge and discharge profiles of uncoated and coated NMCs cycled between 3.0–4.3 V at room temperature (Discharge rate cycle 1: 0.1 C, cycle 10–100: 0.5 C): a) Initial charge and discharge curves, b–e) charge and discharge curves from cycle 10 to 100 in steps of 15 cycles (b: uncoated NMC, c: Al_2O_3 , d: ZrO_2 coated NMC, e: TiO_2 coated NMC), f) evolution of electrochemical polarization voltages during cycling.

voltage peak appears at the very beginning of the charging process, reaching up to 4.1 V. Afterwards, the voltage is decreasing to approx. 3.8 V again, before it increases slowly to 4.3 V. The first charging curve of the uncoated sample lies at higher voltages compared to coated NMCs, indicating a higher resistance. However, the initial voltage peak feature of the uncoated sample is not anymore observed in further cycles. Exactly this phenomenon was observed by Jung *et al.*^[54] who ran storage tests on high-nickel NMC and investigated the influence on the cycling performance. The residual lithium on high-nickel NMC surfaces tends to react with humidity and subsequently the initially created surface hydroxides form carbonates via the reaction with CO_2 during storage.^[54,55] These impurities form an insulating and therefore resistive layer, covering the active material particles and result into the higher potential of the charging curve.^[54] The disappearance of the initial voltage peak in subsequent cycles indicates decomposition of the impurities during the first charge.^[54] In contrast, for the coated samples no initial voltage peak and a lower potential in the charging curve is observed; delithiation of NMC starts at approx. 3.7 V. This indicates that no significant amount of surface impurities is present on the coated samples. Please note that the fresh NMC material was coated and the uncoated and coated NMCs were stored for several weeks before they were used for this study. Consequently, the coating layers successfully shielded the surfaces of NMC during storage.

The comparison of first cycle coulombic efficiencies reveals that the highest irreversible capacity loss of 22% was observed for uncoated NMC. The Al_2O_3 coated sample shows only a loss of 13%, while for ZrO_2 and TiO_2 coatings losses of 17% and 14% were observed. The lower initial coulombic efficiency of uncoated NMC resulted from a decreased discharge capacity, caused by the decomposition of surface impurities like Li_2CO_3 and LiOH on the uncoated NMC surface, leading to the irreversible capacity loss. After their decomposition in the first

charging step, the contained lithium was obviously lost and could not take part in the cycling process anymore. It is important to consider that the formation of a SEI layer also on the anode side contributes to the irreversible capacity loss.

Upon cycling, the discharge capacity of uncoated NMC (Figure 10b) decreases at a faster rate than that of Al_2O_3 (Figure 10c), ZrO_2 (Figure 10d) and TiO_2 coated NMC (Figure 10e). Moreover, there is a voltage drop at the beginning of each discharging step, growing with increasing cycle number (marked with circle in Figure 10). The change of the polarization voltage over the cycles is illustrated in Figure 10f. In the initial cycles the increase of polarization voltage is stronger for all samples, while it stabilizes to a certain degree after about 9 cycles. This phenomenon could be attributed to the formation and activation of the SEI. As the number of cycles increase, the uncoated NMC discharge potential decreases greatly with large electrochemical polarization, while those of the coated NMCs exhibit an improved trend. It clearly shows that Al_2O_3 , ZrO_2 and TiO_2 coatings can play a major role in suppressing electrochemical polarization. The trend which was observed in the long-term cycling stability test is consistent with the electrochemical polarization evaluation. The Al_2O_3 coating obviously shows the best effect on stabilizing high-nickel NMC, showing the lowest and most constant polarization over the cycles (~ 0.05 V after 100 cycles). The ZrO_2 and TiO_2 coated samples show almost the same polarization voltage after 100 cycles (~ 0.16 V). In comparison to TiO_2 coated NMC, the polarization voltage for ZrO_2 coating is lower in cycle numbers < 100 , but the slope of the polarization voltage increase is slightly higher for ZrO_2 , so it would exceed the curve of TiO_2 shortly after cycle 100. For the TiO_2 coated NMC a strong polarization voltage increase is observed in the initial cycles, almost as strong as for the uncoated sample, but after cycle 9 a stabilization occurs. After the stabilization, the polarization

voltage increase of TiO_2 -coated NMC is significantly lower than for uncoated NMC (~ 0.25 V after 100 cycles).

In general, the extent of polarization is closely related to the interfacial properties.^[70] It is well known that decomposition of electrolyte on the electrode surface causes capacity degradation and increase in charge transfer resistance.^[71] Additionally, impurity phases on high-nickel NMC surfaces, mostly carbonates with minor fractions of hydroxides and water not only lead to faster capacity fading, but also increase the impedance of the NMC cathode.^[54] The decomposition of LiPF_6 by trace amounts of water leads to a release of corrosive HF and inactive LiF.^[72] These side reactions increase the charge transfer resistance and the LiF phase formed on the electrode surface is highly resistive to lithium ion migration,^[73] resulting in a capacity and voltage fading. Uncoated NMC shows the highest slope of electrochemical polarization, indicating severe polarization caused by side reactions and a steady growth of a thick SEI-layer with large resistance.^[74,75] The reduction of electrochemical polarization voltage evolution during cycling by the applied coatings confirms the successful suppression of the interfacial side reactions between the cathode materials and electrolyte, reducing the interfacial resistance.

The voltage vs. capacity profiles show how the discharge capacity and also the medium discharge voltage are decreasing over the cycles (Figure 10). The area under the discharge plot can be correlated to the output energy delivered by the battery. The order of the achieved output energy for the samples is $\text{Al}_2\text{O}_3 > \text{ZrO}_2 > \text{TiO}_2$ coated NMC > uncoated NMC (until cycle 100). The detailed discharge capacities, medium discharge voltages and the corresponding output energies at cycle 100 are listed in Table 2.

2.5. Analytical Characterization of Cycled Electrodes

2.5.1. Effects of coatings on NMC cracking

SEM-EDX images of cross sections of cycled electrodes are shown in Figure 11. In the BSE image of the electrode containing the fumed Al_2O_3 -coated NMC (Figure 11a), it can be seen that NMC particles are still intact, even after extensive cycling (250 cycles). The SEM-EDX mapping of Al (Figure 11b) reveals that the fumed Al_2O_3 coating layer is still at the surface of each cathode material particle and intact. In case of the ZrO_2 coated NMC (Figure 11c,d) significantly stronger crack formation is observed, whereas within the TiO_2 coated samples (Figure 11e,f), only moderate crack formation is detected. In both samples the fumed metal oxide coating layers remained

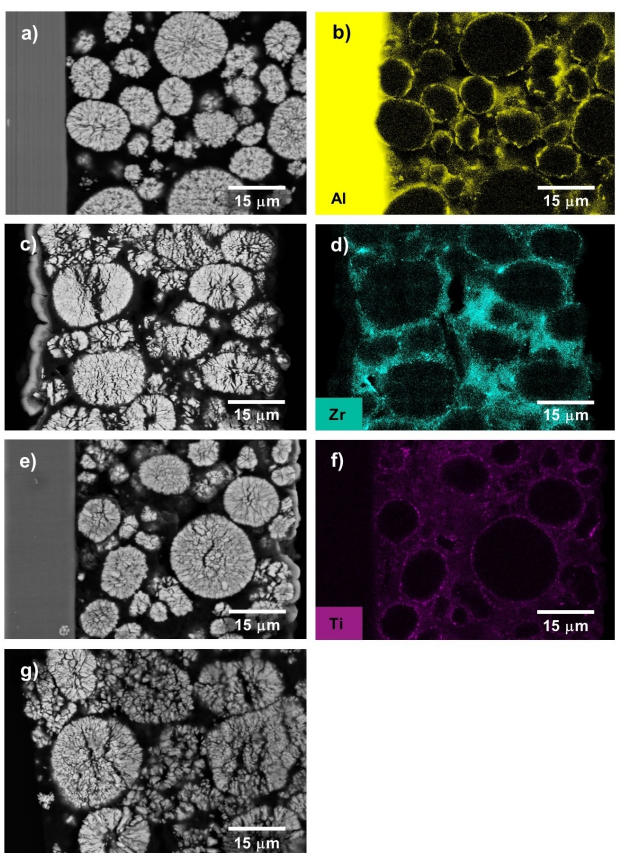


Figure 11. SEM-EDX images of cross sections of cycled electrodes after 250 cycles of Al_2O_3 (a: BSE, b: EDX image), ZrO_2 (c: BSE, d: EDX image; current collector was detached during sample preparation process), TiO_2 coated NMC (e: BSE, f: EDX image) and uncoated NMC (g: BSE image; current collector detached).

mostly intact. This demonstrates that all dry coated fumed metal oxide coating layers remain not only stable during slurry preparation and cathode manufacturing, but they also remain intact during extensive battery cycling.

In contrast, severe crack formation and particle disintegration was detected in the uncoated NMC electrode after cycling (Figure 11g). Most of the secondary particles fragmented completely into primary crystallites, generating new surfaces for further electrolyte decomposition and SEI formation, caused by the increase in surface area of cathode material, which is exposed to the electrolyte. The consequence is further impedance increase, degradation of performance and capacity fade. Additionally, the loss of inner particle connectivity is giving rise to increased polarization as can be seen in Figure 10f.^[1]

Table 2. Discharge capacities, medium discharge voltages and corresponding output energies at cycle 100 for the uncoated and coated NMCs.

	Discharge capacities [mAh/g]	Medium discharge voltage [V]	Output energy [mWh/g]
Uncoated NMC	97.6	3.61	352
Al_2O_3 coated NMC	154.2	3.76	580
ZrO_2 coated NMC	137.1	3.70	508
TiO_2 coated NMC	130.8	3.68	482

It is known that liquid electrolyte permeates and penetrates along grain boundaries in the secondary particle structure of CAMs,^[28,76,77] and that reaction between CAM and liquid electrolyte leads to the formation of species such as Li_2CO_3 , LiF and PO_xF_y .^[78,79] The formation of these species results in consumption of electrolyte, depletion of conducting salt in the electrolyte and formation of a thick SEI layer on the surface and along the grain boundaries of the cathode particles.^[77] Thickening of SEI along grain boundaries, as well as the layered to spinel/rock-salt phase transformation that can be observed in the surface areas of grains during cycling and transition metal migration to lithium sites is causing more and more mechanical stress in the secondary particle structure.^[28,77,80] These high energy boundaries, that are strongly strained during cycling, appear to induce intergranular crack formation in the secondary particle structure.^[28,80] Subsequently, prolonged cycling will lead to fracture and disintegration of the active materials secondary particles along the grain boundaries.^[81] This leads to a self-amplification of the problems associated with solid-liquid reaction due to a continuous increase in surface area and hence more active sites for parasitic reactions.^[76,78,81]

Since the coverage of these reactive sites (i.e., the grain boundary regions at the particle surfaces) by fumed metal oxides in our dry coating approach is especially high, it can be expected that the coating material on top of the grain boundaries impedes the penetration of the electrolyte to a certain degree. Please note, that the coating layers are not consistently porous, due to a certain densification and coalescence of the coating particles on the surface. Even more important is that the coating materials effectively prevent the diffusion of HF inside the vulnerable grain boundaries due to their remarkable HF-scavenging abilities. According to Edström *et al.* it is especially important to reduce the impact of HF on the electrode surface chemistry.^[82] The highly acidic HF dissolves transition metal ions out of the surface of the cathode material into the electrolyte, causing lattice distortion in the cathode material and consequently crack initiation.^[2,3,6,7]

Furthermore, Börner *et al.*^[83] demonstrated that local inhomogeneities, which are always present in cathodes, lead to overcharge conditions driven by local inhomogeneity in SOC and current densities. Beyond that, accelerated kinetics on the surface^[84] or at grain boundaries^[85] lead to a highly delithiated structure on the surface of each primary particle within the secondary particles.^[83] Due to a repulsive interaction of adjacent transition metal oxide layers and the formation of new phases with larger lattice parameters, like the spinel structure that forms as a result of the transition metal migration in the highly delithiated NMC, the highly delithiated areas suffer from anisotropic stress.^[83,84,86–89] This will cause discrete particle cracking which is accompanied with the detachment of particle fractions and capacity fading due to the loss of electric contact.^[83,90,91] This degradation is significantly more pronounced with increasing C-rates due to the higher impact of local inhomogeneity on local current densities and potentials.^[83] Our coating layers may help to mitigate this phenomenon by improving the conductivity of the cathode, what can be derived from the significant enhancement in the

rate performances of the coated samples. This should reduce local inhomogeneity in SOC and current densities in the electrode.

Besides these effects, the coating layers can also act as a kind of adhesive glue, holding the outer sphere of the secondary particle structure together. Since the physical interactions are strong enough to keep the dry coated particles attached to the CAM surface, even under the shear forces during cathode slurry preparation and subsequent calendering in the cathode manufacturing process, this impact should not be underestimated but cannot be quantified. Tsai *et al.*^[92] clearly demonstrated that a thin surface layer of binder is sufficient to prevent the disintegration that occurs for unconstrained high-nickel CAM particles. Although radial cracks still appear, these cracks are not open to the surface of the particle and particle separation is not observed.

We conclude that dry coated layers made from fumed metal oxides are able to successfully protect surfaces of high-nickel cathode materials from detrimental side reactions, reduce crack formation and particle disintegration. The observed protective trend from the investigation of cycled electrodes is $\text{Al}_2\text{O}_3 > \text{TiO}_2 > \text{ZrO}_2$, which confirms the results of the long-term cycling test in the electrochemical evaluation section.

2.5.2. Reactions of coatings during cycling

X-ray photoelectron spectroscopy (XPS) analysis was performed to investigate whether lithium ions enter into the fumed ZrO_2 and TiO_2 layers, like it was observed in fumed Al_2O_3 coatings in our previous work.^[45] Figure 12 shows XPS data of cycled electrodes containing ZrO_2 coated NMC and TiO_2 coated NMC. In the $\text{Li}1s$ -spectrum of cycled ZrO_2 coated NMC and cycled TiO_2 coated NMC a signal at 54.7 eV is detected, which is identical to the signal of lithium zirconate and lithium titanate reference samples, respectively. Furthermore, in both samples a peak at 55.8 eV is detected and identified as LiF by comparison with a commercial reference sample. The signals at 53.9 eV, detected at both samples, correspond to the signal of fresh ground bare NMC701515.

Additionally, in Figure 12 $\text{Zr}2p$ and $\text{Ti}2p$ spectra of uncycled and cycled coated electrodes are compared to lithium zirconate and lithium titanate spectra of reference compounds. For both, $\text{Zr}2p$ and $\text{Ti}2p$ signals, a small shift towards lower binding energy of the cycled electrodes, compared to the uncycled samples, is observed. The signals are in between the signals of the uncycled samples and the fully lithiated reference compounds, giving a strong hint that both coatings are partially lithiated to $\text{Li}_x\text{ZrO}_{2+0.5x}$ and $\text{Li}_x\text{TiO}_{2+0.5x}$ like it was observed for fumed $\gamma\text{-Al}_2\text{O}_3$ coating layers.^[45]

Since XPS-measurements indicate the partial formation of $\text{Li}_x\text{ZrO}_{2+0.5x}$ and $\text{Li}_x\text{TiO}_{2+0.5x}$, we assume incorporation of lithium ions also in fumed ZrO_2 and TiO_2 coating layers during cycling. This would contribute to the increased rate performance and lithium ion diffusivity in the electrode and could explain the

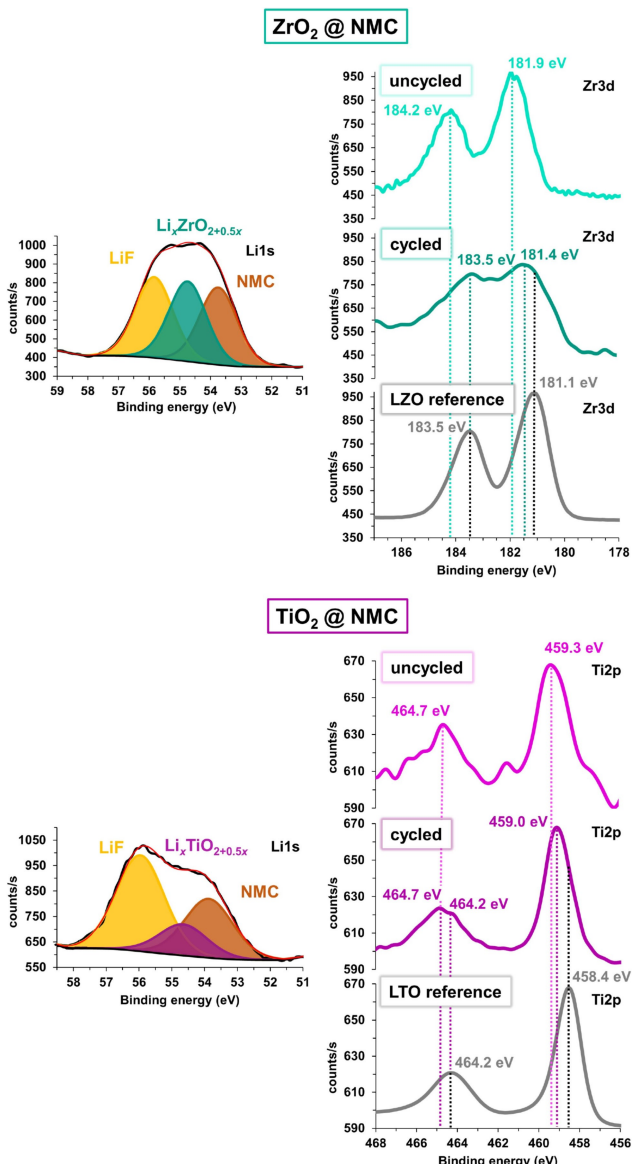


Figure 12. XPS analysis of cycled electrodes containing ZrO₂ coated NMC and TiO₂ coated NMC. Top: Li1s spectrum of cycled ZrO₂ coated NMC and Zr3d spectra of uncycled and cycled ZrO₂ coated NMC, compared to the reference spectrum of lithium zirconate (LZO); Bottom: Li1s spectrum of cycled TiO₂ coated NMC and Ti2p spectra of uncycled and cycled TiO₂ coated NMC, compared to the reference spectrum of lithium titanate (LTO).

significantly improved rate performance of ZrO₂ and TiO₂ coated NMC, observed in the electrochemical evaluation.

We assume that lithium ion migration across the partly porous coating layer is proceeding through preferred paths with the lowest resistance and only here the lithium ions interact with the coating layers, like it was observed for fumed Al₂O₃ coatings.^[45] Along these paths, the lithium diffusivity is enhanced permanently in Li_xZrO_{2+0.5x} compared to ZrO₂ and Li_xTiO_{2+0.5x} compared to TiO₂.^[93–95]

3. Conclusions

Nanostructured fumed Al₂O₃, TiO₂ and ZrO₂ were coated successfully by dry powder high energy mixing on high-nickel NMC. The different fumed metal oxides were processed equally; no significant differences in mixing intensity and time for coating procedure were observed. The small nanostructured aggregate sizes result in a quite homogeneous coating layer around each cathode active material particle. After dry coating, no sintering process was applied to fix the particles, and the coating layers remain intact during the cathode manufacturing process. A beneficial side effect of the coating layers is that hydroxide and carbonate surface impurity formation on high-nickel materials during storage appears to be prevented. For each coated NMC a significantly enhanced long-term cycling stability was observed. The trend is ZrO₂<TiO₂<Al₂O₃. This trend is supported by investigations of cross sections of cycled electrodes, revealing that Al₂O₃ and TiO₂ coating layers prevent cathode particle cracking and disintegration successfully, while the ZrO₂ coating shows only moderate protection. Since the Al₂O₃ coating layer shows not the best physical parameters for the long-term cycling stability (highest surface coverage) among the tested coating agents, its higher protective effect of high-nickel NMC surfaces from detrimental side reactions is attributed to the superior chemical nature of Al₂O₃. Additionally, this is supported by voltage-capacity profiles, showing that the best voltage fade improvement during cycling is achieved for Al₂O₃ coatings. Due to different physical parameters (degrees of surface coverage) of the ZrO₂ and TiO₂ coating layers, it is hard to conclude which material has the best chemical properties for protecting the surface of NMC. Therefore, this will be investigated in further studies.

Furthermore, each coating material distinctly enhances the rate performance compared to uncoated NMC in the row Al₂O₃>ZrO₂>TiO₂. XPS measurements of cycled electrodes indicate partial incorporation of lithium ions in the crystalline TiO₂ and ZrO₂ coating layers, contributing to the enhanced lithium transport across the CAM surface layer, like it was observed for fumed γ-Al₂O₃ coatings before.^[45] Furthermore, it seems that the physical parameter of coating layer porosity, which is influenced by the BET surface area of the coating agent, has, besides the chemical composition of the coating material, a significant effect on the rate capability of the coated CAMs. Since lithium zirconate is attributed a significantly higher lithium ion conductivity than γ-lithium aluminate,^[57,58] the lower rate performance of the ZrO₂ coated NMC arises from the inferior physical properties of the coating layer. It is very likely that, when these materials have the same porosity, the rate performance of ZrO₂-coated NMC will be superior. However, this parameter can only be optimized in the fumed particle synthesis, which requires further work in the future. By contrast, the superior rate performance of the Al₂O₃ coated NMC compared to the TiO₂ coated sample can clearly be attributed to the favourable chemical properties of Al₂O₃. In terms of rate performance, ZrO₂ is attributed favorable chemical properties compared to TiO₂.

The best overall cycling performance of coated high-nickel NMC was achieved by coating with fumed Al_2O_3 , providing the highest rate capability and long-term cycling stability. Fumed ZrO_2 and TiO_2 coatings also improve the cycling performance of NMC significantly, whereby ZrO_2 leads to higher rate performance and TiO_2 to higher long-term cycling stability, compared to each other.

In conclusion, the developed dry coating process is a very effective method to protect the surface and enhance the performance of CAMs. The process is easily scalable to large scale high intensity mixers and therefore suitable for industrial manufacturing. Furthermore, the coating process can be transferred to other types of CAMs. Other metal oxides are under investigation as potential coating agents.

Acknowledgments

The authors would like to thank Erik Peldszus and Steve Rienecker for the support of scanning electron microscopy and X-ray photoelectron spectroscopy analysis. We acknowledge support of the Institute of Electron Microscopy for Materials Science of the University of Antwerp in the TEM measurements. Open access funding enabled and organized by Projekt DEAL.

Conflict of Interest

The authors declare no conflict of interest.

Keywords: cathode active material • lithium-ion battery • dry coating • capacity fading • nanostructured oxide • fumed metal oxide

- [1] W. Liu, P. Oh, X. Liu, M.-J. Lee, W. Cho, S. Chae, Y. Kim, J. Cho, *Angew. Chem. Int. Ed.* **2015**, *54*, 4440–4457.
- [2] Y. Oh, S. Nam, S. Wi, S. Hong, B. Park, *Electron. Mater. Lett.* **2012**, *8*, 91–105.
- [3] A. Mauger, C. Julien, *Ionics* **2014**, *20*, 751–787.
- [4] G. E. Blomgren, *J. Electrochem. Soc.* **2017**, *164*, A5019–A5025.
- [5] X. Xiong, Z. Wang, G. Yan, H. Guo, X. Li, *J. Power Sources* **2014**, *245*, 183–193.
- [6] Y. J. Kim, J. Cho, T.-J. Kim, B. Parka, *J. Electrochem. Soc.* **2003**, *150*, A1723–A1725.
- [7] J. L. Tebbe, A. M. Holder, C. B. Musgrave, *ACS Appl. Mater. Interfaces* **2015**, *7*, 24265–24278.
- [8] J. Zheng, P. Yan, J. Zhang, M. H. Engelhard, Z. Zhu, B. J. Polzin, S. Trask, J. Xiao, C. Wang, J. Zhang, *Nano Res.* **2017**, *10*, 4221–4231.
- [9] S.-K. Jung, H. Gwon, J. Hong, K.-Y. Park, D.-H. Seo, H. Kim, J. Hyun, W. Yang, K. Kang, *Adv. Energy Mater.* **2014**, *4*, 1300787.
- [10] B. Wu, J. Bi, Q. Liu, D. Mu, L. Wang, J. Fu, F. Wu, *Electrochim. Acta* **2019**, *298*, 609–615.
- [11] K.-S. Lee, S.-T. Myung, K. Amine, H. Yashiro, Y.-K. Sun, *J. Electrochem. Soc.* **2007**, *154*, A971.
- [12] S.-M. Bak, E. Hu, Y. Zhou, X. Yu, S. D. Senanayake, S.-J. Cho, K.-B. Kim, K. Y. Chung, X.-Q. Yang, K.-W. Nam, *ACS Appl. Mater. Interfaces* **2014**, *6*, 22594–22601.
- [13] L. de Biasi, A. O. Kondrakov, H. Geßwein, T. Brezesinski, P. Hartmann, J. Janek, *J. Phys. Chem. C* **2017**, *121*, 26163–26171.
- [14] L. de Biasi, B. Schwarz, T. Brezesinski, P. Hartmann, J. Janek, H. Ehrenberg, *Adv. Mater.* **2019**, *31*, 1900985.
- [15] K. Shizuka, T. Kobayashi, K. Okahara, K. Okamoto, S. Kanzaki, R. Kanno, *J. Power Sources* **2005**, *146*, 589–593.
- [16] L. Xu, F. Zhou, B. Liu, H. Zhou, Q. Zhang, J. Kong, Q. Wang, *Int. J. Electrochem.* **2018**, *2018*, 1–12.
- [17] H. J. Bang, B.-C. Park, J. Prakash, Y.-K. Sun, *J. Power Sources* **2007**, *174*, 565–568.
- [18] F. Schipper, M. Dixit, D. Kovacheva, M. Taliander, O. Haik, J. Grinblat, E. M. Erickson, C. Ghanty, D. T. Major, B. Markovsky, et al., *J. Mater. Chem. A* **2016**, *4*, 16073–16084.
- [19] S.-W. Cho, K.-S. Ryu, *Mater. Chem. Phys.* **2012**, *135*, 533–540.
- [20] D. Wang, X. Li, Z. Wang, H. Guo, Y. Xu, Y. Fan, J. Ru, *Electrochim. Acta* **2016**, *188*, 48–56.
- [21] D. Weber, D. Tripković, K. Kretschmer, M. Bianchini, T. Brezesinski, *Eur. J. Inorg. Chem.* **2020**, DOI 10.1002/ejic.202000408.
- [22] Z. Chen, Y. Qin, K. Amine, Y.-K. Sun, *J. Mater. Chem.* **2010**, *20*, 7606–7612.
- [23] J. Cabana, B. J. Kwon, L. Hu, *Acc. Chem. Res.* **2018**, *51*, 299–308.
- [24] J. Duan, X. Tang, H. Dai, Y. Yang, W. Wu, X. Wei, Y. Huang, *Electrochem. Energ. Rev.* **2020**, *3*, 1–42.
- [25] Y.-K. Sun, S.-T. Myung, M.-H. Kim, J. Prakash, K. Amine, *J. Am. Chem. Soc.* **2005**, *127*, 13411–13418.
- [26] Y.-K. Sun, S.-T. Myung, B.-C. Park, J. Prakash, I. Belharouak, K. Amine, *Nat. Mater.* **2009**, *8*, 320–324.
- [27] A. O. Kondrakov, A. Schmidt, J. Xu, H. Geßwein, R. Möning, P. Hartmann, H. Sommer, T. Brezesinski, J. Janek, *J. Phys. Chem. C* **2017**, *121*, 3286–3294.
- [28] B. Xiao, X. Sun, *Adv. Energy Mater.* **2018**, *8*, 1802057.
- [29] D. Mohanty, K. Dahlberg, D. M. King, L. A. David, A. S. Sefat, D. L. Wood, C. Daniel, S. Dhar, V. Mahajan, M. Lee, F. Albano, *Sci. Rep.* **2016**, *6*, 26532.
- [30] S. Schweißler, L. de Biasi, G. Garcia, A. Mazilkin, P. Hartmann, T. Brezesinski, J. Janek, *ACS Appl. Energy Mater.* **2019**, *2*, 7375–7384.
- [31] S. Dong, Y. Zhou, C. Hai, J. Zeng, Y. Sun, Y. Shen, X. Li, X. Ren, G. Qi, X. Zhang, L. Ma, *Ceram. Int.* **2019**, *45*, 144–152.
- [32] C. Chen, T. Tao, W. Qi, H. Zeng, Y. Wu, B. Liang, Y. Yao, S. Lu, Y. Chen, *J. Alloys Compd.* **2017**, *709*, 708–716.
- [33] K. S. Yoo, Y. H. Kang, K. R. Im, C.-S. Kim, *Materials* **2017**, *10*, 1273.
- [34] A. Yano, A. Ueda, M. Shikano, H. Sakaebe, Z. Ogumi, *J. Electrochem. Soc.* **2016**, *163*, A75–A82.
- [35] M. R. Laskar, D. H. K. Jackson, S. Xu, R. J. Hamers, D. Morgan, T. F. Kuech, *ACS Appl. Mater. Interfaces* **2017**, *9*, 11231–11239.
- [36] J.-Z. Kong, C. Ren, G.-A. Tai, X. Zhang, A.-D. Li, D. Wu, H. Li, F. Zhou, *J. Power Sources* **2014**, *266*, 433–439.
- [37] S. Neudeck, A. Mazilkin, C. Reitz, P. Hartmann, J. Janek, T. Brezesinski, *Sci. Rep.* **2019**, *9*, DOI 10.1038/s41598-019-41767-0.
- [38] P. Sun, Y. Ma, T. Zhai, H. Li, *Electrochim. Acta* **2016**, *191*, 237–246.
- [39] C. Hudaya, J. H. Park, J. K. Lee, W. Choi, *Solid State Ionics* **2014**, *256*, 89–92.
- [40] Q. Hou, G. Cao, P. Wang, D. Zhao, X. Cui, S. Li, C. Li, *J. Alloys Compd.* **2018**, *747*, 796–802.
- [41] L. Su, P. M. Smith, P. Anand, B. Reeja-Jayan, *ACS Appl. Mater. Interfaces* **2018**, *10*, 27063–27073.
- [42] J.-T. Son, *J. Korean Electrochem. Soc.* **2010**, *13*, 246–250.
- [43] J. Yang, A. Sliva, A. Banerjee, R. N. Dave, R. Pfeffer, *Powder Technol.* **2005**, *158*, 21–33.
- [44] R. Pfeffer, R. N. Dave, D. Wei, M. Ramlakhan, *Powder Technol.* **2001**, *117*, 40–67.
- [45] M. J. Herzog, N. Gauquelain, D. Esken, J. Verbeeck, J. Janek, *Energy Technol.* **2021**, DOI 10.1002/ente.202100028.
- [46] S. Neudeck, F. Strauss, G. Garcia, H. Wolf, J. Janek, P. Hartmann, T. Brezesinski, *Chem. Commun.* **2019**, *55*, 2174–2177.
- [47] Y. Chen, Y. Zhang, B. Chen, Z. Wang, C. Lu, *J. Power Sources* **2014**, *256*, 20–27.
- [48] K. Min, K. Park, S. Y. Park, S.-W. Seo, B. Choi, E. Cho, *J. Electrochem. Soc.* **2018**, *165*, A79–A85.
- [49] P. Albers, M. Maier, M. Reisinger, B. Hannebauer, R. Weinand, *Cryst. Res. Technol.* **2015**, *50*, 846–865.
- [50] Y. Ouabbes, A. Chamayou, L. Galet, M. Baron, G. Thomas, P. Grosseau, B. Guilhot, *Powder Technol.* **2009**, *190*, 200–209.
- [51] F. Cavaillès, R. Sescombe, A. Chamayou, L. Galet, *Adv. Powder Technol.* **2017**, *28*, 2875–2885.
- [52] G. Lefebvre, L. Galet, A. Chamayou, *Powder Technol.* **2011**, *208*, 372–377.
- [53] P. Zhou, Z. Zhang, H. Meng, Y. Lu, J. Cao, F. Cheng, Z. Tao, J. Chen, *Nanoscale* **2016**, *8*, 19263–19269.

- [54] R. Jung, R. Morasch, P. Karayaylali, K. Phillips, F. Maglia, C. Stinner, Y. Shao-Horn, H. A. Gasteiger, *J. Electrochem. Soc.* **2018**, *165*, A132–A141.
- [55] J. Sicklinger, M. Metzger, H. Beyer, D. Pritzl, H. A. Gasteiger, *J. Electrochem. Soc.* **2019**, *166*, A2322–2335.
- [56] X. Li, J. Liu, X. Meng, Y. Tang, M. N. Banis, J. Yang, Y. Hu, R. Li, M. Cai, X. Sun, *J. Power Sources* **2014**, *247*, 57–69.
- [57] J. Uhlendorf, B. Ruprecht, E. Witt, C. V. Chandran, L. Dörner, E. Hüger, F. Strauß, P. Heitjans, H. Schmidt, *Z. Phys. Chem.* **2017**, *231*, 1423.
- [58] Y. Dong, Y. Zhao, H. Duan, J. Huang, *Electrochim. Acta* **2015**, *161*, 219–225.
- [59] S.-I. Lee, U.-H. Jung, Y.-S. Kim, M.-H. Kim, D.-J. Ahn, H.-S. Chun, *Korean J. Chem. Eng.* **2002**, *19*, 638–644.
- [60] S. G. Stewart, J. Newman, *J. Electrochem. Soc.* **2008**, *155*, F13.
- [61] S. Takai, M. Kamata, S. Fujine, K. Yoneda, K. Kanda, T. Esaka, *Solid State Ionics* **1999**, *123*, 165–172.
- [62] J. Liu, Q. Wang, B. Reeja-Jayan, A. Manthiram, *Electrochem. Commun.* **2010**, *12*, 750–753.
- [63] S. J. Shi, Y. J. Mai, Y. Y. Tang, C. D. Gu, X. L. Wang, J. P. Tu, *Electrochim. Acta* **2012**, *77*, 39–46.
- [64] M. Aykol, S. Kirklin, C. Wolverton, *Adv. Energy Mater.* **2014**, *4*, 1400690.
- [65] A. K. Haridas, Q. A. Nguyen, B. F. Song, R. Blaser, S. L. Biswal, *ACS Appl. Energy Mater.* **2020**, *3*, 456–468.
- [66] C. Qin, J. Cao, J. Chen, G. Dai, T. Wu, Y. Chen, Y. Tang, A. Li, Y. Chen, *Dalton Trans.* **2016**, *45*, 9669–9675.
- [67] J.-S. Kim, C. S. Johnson, J. T. Vaughan, S. A. Hackney, K. A. Walz, W. A. Zeltner, M. A. Anderson, M. M. Thackeraya, *J. Electrochem. Soc.* **2004**, *151*, A1755–A1761.
- [68] X. Zhu, C. S. Ong, X. Xu, B. Hu, J. Shang, H. Yang, S. Katlakunta, Y. Liu, X. Chen, L. Pan, et al., *Sci. Rep.* **2013**, *3*, DOI DOI 10.1038/srep01084.
- [69] H. Moriwake, A. Kuwabara, C. A. J. Fisher, R. Huang, T. Hitosugi, Y. H. Ikuhara, H. Oki, Y. Ikuhara, *Adv. Mater.* **2013**, *25*, 618–622.
- [70] B. Lei, J. Yang, Z. Xu, S. Su, D. Wang, *Chem. Commun.* **2018**, *54*, 13567–13570.
- [71] T. Osaka, D. Mukoyama, H. Nara, *J. Electrochem. Soc.* **2015**, *14*, A2529–A2537.
- [72] L. Li, Z. Chen, Q. Zhang, M. Xu, X. Zhou, H. Zhu, K. Zhang, *J. Mater. Chem. A* **2015**, *3*, 894–904.
- [73] J. S. Gnanaraj, E. Zinigrad, M. D. Levi, D. Aurbach, M. Schmidt, *J. Power Sources* **2003**, *119–121*, 799–804.
- [74] J. Shim, R. Kostecki, T. Richardson, X. Song, K. A. Striebel, *J. Power Sources* **2002**, *112*, 222–230.
- [75] R. Jorn, R. Kumar, D. P. Abraham, G. A. Voth, *J. Phys. Chem. C* **2013**, *117*, 3747–3761.
- [76] P. Yang, J. Zheng, S. Kuppan, Q. Li, D. Lv, J. Xiao, G. Chen, J.-G. Zhang, C.-M. Wang, *Chem. Mater.* **2015**, *27*, 7447–7451.
- [77] P. Yan, J. Zheng, J. Liu, B. Wang, X. Sun, C. Wang, J.-G. Zhang, *Nat. Energy* **2018**, *3*, 600–605.
- [78] K. Xu, *Chem. Rev.* **2014**, *114*, 11503–11618.
- [79] R. Naejus, D. Lemordant, R. Coudert, P. Willmann, *J. Fluorine Chem.* **1998**, *90*, 81–85.
- [80] S. Sharifi-Asl, V. Yurkiv, A. Gutierrez, M. Cheng, M. Balasubramanian, F. Mashayek, J. Croy, R. Shahbazian-Yassar, *Nano Lett.* **2020**, *20*, 1208–1217.
- [81] F. Schipper, E. M. Erickson, C. Erk, J.-Y. Shin, F. F. Chesneau, D. Aurbach, *J. Electrochem. Soc.* **2017**, *164*, A6220–A6221.
- [82] K. Edström, T. Gustafsson, J. O. Thomas, *Electrochim. Acta* **2004**, *50*, 397–403.
- [83] M. Börner, F. Horsthemke, F. Kollmer, S. Haseloff, A. Friesen, P. Niehoff, S. Nowak, M. Winter, F. M. Schappacher, *J. Power Sources* **2016**, *335*, 45–55.
- [84] S. Hwang, W. Chang, S. M. Kim, D. Su, D. H. Kim, J. Y. Lee, K. Y. Chung, E. A. Stach, *Chem. Mater.* **2014**, *26*, 1084–1092.
- [85] S. Han, J. Park, W. Lu, A. M. Sastry, *J. Power Sources* **2013**, *240*, 155–167.
- [86] C. Julien, *Solid State Ionics* **2000**, *136–137*, 887–896.
- [87] M. Winter, J. O. Besenhard, M. E. Spahr, P. Novák, *Adv. Mater.* **1998**, *10*, 725–763.
- [88] M. Kerlau, M. Marcinek, V. Srinivasan, R. M. Kostecki, *Electrochim. Acta* **2007**, *52*, 5422–5429.
- [89] R. E. Ruther, A. F. Callender, H. Zhou, S. K. Martha, J. Nanda, *J. Electrochem. Soc.* **2015**, *162*, A98–A102.
- [90] J. Vetter, P. Novák, M. R. Wagner, C. Veit, K.-C. Möller, J. O. Besenhard, M. Winter, M. Wohlfahrt-Mehrens, C. Vogler, A. Hammouche, *J. Power Sources* **2005**, *147*, 269–281.
- [91] H. Wang, Y. -I Jang, B. Huang, D. R. Sadoway, Y. -M Chiang, *J. Electrochem. Soc.* **1999**, *146*, 473.
- [92] P.-C. Tsai, B. Wen, M. Wolfman, M.-J. Choe, M. S. Pan, L. Su, K. Thornton, J. Cabana, Y.-M. Chiang, *Energy Environ. Sci.* **2018**, *11*, 860–871.
- [93] S. Ito, S. Fujiki, T. Yamada, Y. Aihara, Y. Park, T. Y. Kim, S.-W. Baek, J.-M. Lee, S. Doo, N. Machida, *J. Power Sources* **2014**, *248*, 943–950.
- [94] J. Zhang, Z. Li, R. Gao, Z. Hu, X. Liu, *J. Phys. Chem. C* **2015**, *119*, 20350–20356.
- [95] J.-H. Shim, J. Lee, S. Y. Han, S. Lee, *Electrochim. Acta* **2015**, *186*, 201–208.

Manuscript received: January 18, 2021

Revised manuscript received: February 10, 2021

Accepted manuscript online: February 15, 2021

Version of record online: February 23, 2021